Lattice strain effects on the finite-temperature magnetism of two-dimensional single-layer CrI_3

Dongqi Luo, Weishan Xue, Xihui Yang, Yu Ni, Zhe Yuan, Yi Liu,* and Yun Song†
Center for Advanced Quantum Studies and Department of Physics, Beijing Normal University, Beijing 100875, China

(Received 21 April 2023; revised 9 July 2023; accepted 15 September 2023; published 25 September 2023)

The magnetic properties of two-dimensional single-layer CrI_3 at finite temperatures are self-consistently calculated within the nonlinear spin wave formalism, where the Heisenberg exchange interaction and the single-ion magnetic anisotropy energy are calculated from first principles. The lattice strain modulates the exchange interactions and determines the magnetic ground state of the single-layer CrI_3 as the ferromagnetic or antiferromagnetic configuration. In both cases, the magnon-magnon interaction at finite temperature softens the magnon spectra. The Curie temperature for the ferromagnetic state varies nonmonotonically with decreasing lattice constant, and the maximum value appears at the compressive strain of -2.1%. The Néel temperature for the antiferromagnetic order linearly increases with increasing compressive strain. The exchange interactions between the next-nearest and third-nearest-neighbor spins are found to play an important role in magnetism. Neglecting these exchange interactions results in a significant deviation in estimating the critical temperature.

DOI: 10.1103/PhysRevB.108.094432

I. INTRODUCTION

Recently discovered two-dimensional (2D) magnetic materials [1–6] open up an exciting arena for fundamental investigations and promising applications. These atomically thin layers favor strong perpendicular magnetic anisotropy that overwhelms thermal fluctuations, which were predicted to rule out any long-range magnetic order at finite temperatures in 2D materials according to the Mermin-Wagner theorem [7]. This long-range magnetic order breaks the time-reversal symmetry of these materials, leading to the emergence of some unique quantum states, such as the intrinsic quantum anomalous Hall state [8,9], giant valley splitting [10], and the half-excitonic insulator [11]. To create more opportunities for applications in spintronics and nanoelectronics, various approaches, such as applying an external electric field [4,12–17], strain [14,18–29], and stacking [27,30], have been employed to manipulate the anisotropy and in turn the magnetic properties. Stacking, as well as substrates on which 2D FM materials are grown, usually imposes strain on 2D FM materials owing to the lattice mismatch. Therefore, it is necessary to comprehensively understand the dependence of the magnetic properties of 2D FM materials on the lattice strain.

For the purpose of applications, which are carried out at finite temperatures, one has to consider the temperature dependence of the magnetic properties of 2D magnetic materials [31]. Being able to precisely evaluate these temperature-dependent magnetic properties has been a general research interest. Much effort has been devoted to developing effective methods for calculating them. The Ising model, with an analytical solution for 2D magnetism, readily applies to 2D magnetic systems. It is, however, restricted to within the limit of infinite single-ion anisotropy and thus provides the upper bound for the Curie temperature [32,33]. Mean-field theory, although it gives a reasonably good description of finite-temperature magnetism in three-dimensional FM metals [34], neglects atomic fluctuations and cannot characterize the collective excitation of spins at low temperatures. These disadvantages are inevitable in its application to 2D magnetic systems [18,35,36]. Monte Carlo (MC) simulations are often employed in theoretical studies of 2D magnetic materials [37–45], where finite anisotropy and atomic fluctuations are treated on an equal footing. Nonlinear spin-wave theory (NLSWT), or renormalized spin-wave theory (RSWT) [46–55], with a much smaller computational cost than MC simulations, provides another effective method to study 2D magnetic systems.

As an extension of the standard linear spin-wave theory (LSWT), NLSWT introduces the magnon-magnon interaction by including higher-order terms in the Hamiltonian [56]. The excitation of magnons, whose distribution is subject to Bose-Einstein statistics, results in demagnetization at finite temperatures. By self-consistently solving the magnon Hamiltonian, one can determine the magnon spectrum at a given temperature and corresponding magnetization. The latter vanishes at the critical temperature. Characteristic parameters of the system, such as the magnetic anisotropy that helps the 2D long-range magnetic order survive at finite temperatures and the Heisenberg exchange interaction that describes the coupling between atomic spins, are essential in NLSWT. Reliable evaluation of them, in this study, is provided through first-principles calculations based on the electronic structure of the materials.

In this paper, taking single-layer CrI_3 as an example, we carry out first-principles total energy calculations for different collinear spin configurations [57] and determine the Heisenberg exchange coefficients and single-ion magnetic anisotropy energy. Feeding these parameters into the NLSWT formalism,

*yiliu@bnu.edu.cn
†yunsong@bnu.edu.cn

 ©2023 American Physical Society

we obtain the magnon spectra as a function of temperature and the related temperature-dependent magnetic properties. Previous studies have shown that single-layer CrI_3 is soft (Young's modulus of 24 Nm^{-1}) [37] compared with other 2D materials, such as FeSe (80 Nm^{-1}) [28] and MoS_2 (180 Nm^{-1}) [58]. We systematically investigate the lattice strain effects on the magnetic properties at various temperatures below the critical temperature. As compressive strain changes the ground state of single-layer CrI_3 from the FM to AFM state, we extend the application of the NLSWT formalism to AFM CrI_3 and study, as in the FM case, the magnon spectra and related properties. We find that the Curie temperature T_C of FM CrI_3 varies nonmonotonically with the lattice strain, with the maximum $T_C = 57$ K appearing at the compressive strain of -2.1%, and the Néel temperature T_N of AFM CrI_3 linearly increases with lattice strain. Ignoring exchange interactions between the next-nearest and/or third-nearest neighbors leads to a significant deviation in the evaluation of the critical temperature.

The rest of this paper is organized as follows. In Sec. II the first-principles calculations are detailed, and the material parameters needed in NLSWT are presented as a function of the lattice strain. The NLSWT method is derived in Sec. III for a single-layer honeycomb lattice in the FM and AFM states. The calculated magnon spectra, demagnetization, and other magnetic properties at finite temperatures within NLSWT are presented and discussed in Sec. IV. A brief summary is given in Sec. V. Appendix A provides the detailed derivation of the magnon Hamiltonians for both the FM and AFM configurations. Fewer exchange interaction terms are explicitly examined in Appendix B.

II. FIRST-PRINCIPLES CALCULATIONS

CrI_3 is a newly found ferromagnetic van der Waals (vdW) insulator [16]. The weak vdW bonding facilitates extraction of thin layers down to atomic thicknesses, where strong magnetocrystalline anisotropy protects long-range magnetic order. As schematically shown in Fig. 1, there are two types of chromium atoms occupying inequivalent Wyckoff sites, marked as Cr_A and Cr_B, forming a honeycomb lattice. Each Cr atom is surrounded by six iodine atoms forming a slightly warped octahedron. Atomic magnetization is localized on Cr atoms. The exchange interactions between Cr atoms are denoted as J_1, J_2, and J_3, representing the interactions between the nearest, next-nearest, and third-nearest neighbors, respectively.

To evaluate the exchange interaction, we first map the total energy of the single-layer CrI_3 system to two terms,

$$E_{\text{tot}} = E_0 + \frac{1}{2}\sum_{i\neq j} J_{ij}\mathbf{S}_i \cdot \mathbf{S}_j, \tag{1}$$

where E_0 is the energy of the system excluding spin-spin interactions and $\mathbf{S}_i$ is the atomic spin of the ith Cr atom with magnitude $S = 3/2$. The total energy is calculated using density functional theory implemented in the Vienna *ab initio* simulation package (VASP) [59,60]. The Perdew-Burke-Ernzerhof [61] functional is employed to describe the exchange and correlation. The PBE version of the all-electron projector augmented wave [62,63] potential is adopted, with

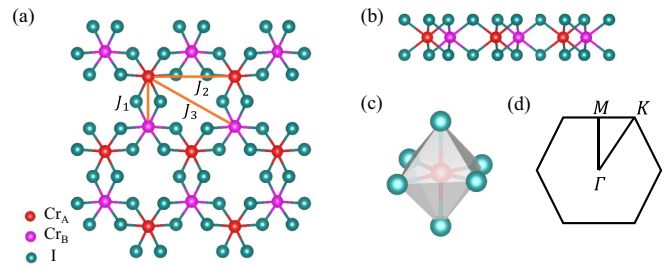

FIG. 1. Schematic illustration of the lattice structure of monolayer CrI_3, top view (a) and side view (b), and of an octahedron formed by eight I atoms around every Cr atom (c). The Heisenberg exchange interactions between the nearest, next-nearest, and third-nearest neighbors are denoted by J_1, J_2, and J_3, respectively (orange line). (d) First Brillouin zone of CrI_3 with high symmetry points.

the $3p^6 3d^5 4s^1$ states of chromium and $4d^{10}5s^2 5p^2$ states of iodine treated as valence electrons. The plane-wave basis set is truncated with a cutoff energy of 600 eV, and the k points in the BZ are sampled with a $10 \times 10 \times 1$ mesh using the Monkhorst-Pack scheme [64]. In the calculations, lattice structures are fully relaxed until the residual interatomic forces are below 0.01 eV/Å.

The Heisenberg exchange interaction J_{ij} is a short-range term, and we consider only the interactions up to the third-nearest neighbor, as denoted in Fig. 1. A 2×2 supercell of CrI_3 within which the atomic magnetizations of different Cr atoms are artificially flipped is employed, and the total energies of 11 inequivalent spin configurations are calculated. Linear regressions of these total energies are carried out to extract the J coefficients [57]. We determine for the original CrI_3 lattice the Heisenberg exchange interaction coefficients as $J_1 = -2.94 \pm 0.04$ meV, $J_2 = -0.62 \pm 0.02$ meV, and $J_3 = 0.16 \pm 0.02$ meV, with good agreement with reported values in the literature [18,28,37,65,66].

Before the exchange interaction as a function of strain is discussed, it is worth mentioning that the change in the nonmagnetic energy E_0, as shown in the inset of Fig. 2(a), induced by strain is three orders of magnitude larger. By checking the energy bands and atomic magnetizations with respect to strain, we confirm that such large strain-induced energy does not lead to insulator-metal phase transition, and the atomic moments keep nearly unchanged. One is allowed to study the magnetic properties in the 2D CrI_3 for strain within the range from -10% to 10%. To ensure that the lattice can sustain such strain range is checked by comparing the values of Young's modulus of 2D materials, such as FeSe [28], MoS_2 [58], and CrI_3 [37] and experimentally realized strain on FeSe (6%) [67,68] and MoS_2 (11%) [58].

With biaxial lattice strain exerted on CrI_3, the exchange parameters vary with the strain, as shown in Fig. 2(a). J_1 is the dominant exchange interaction in the 2D CrI_3 lattice and shows nonmonotonic behavior as the strain changes. It is not very sensitive to tensile (positive) strain but rapidly increases under compressive (negative) strain. At a strain of approximately -6.2%, J_1 changes sign. In contrast, J_2 and J_3 monotonically decrease as the distance between Cr atoms increases, and $J_2 < 0$ and $J_3 > 0$ hold for the whole strain

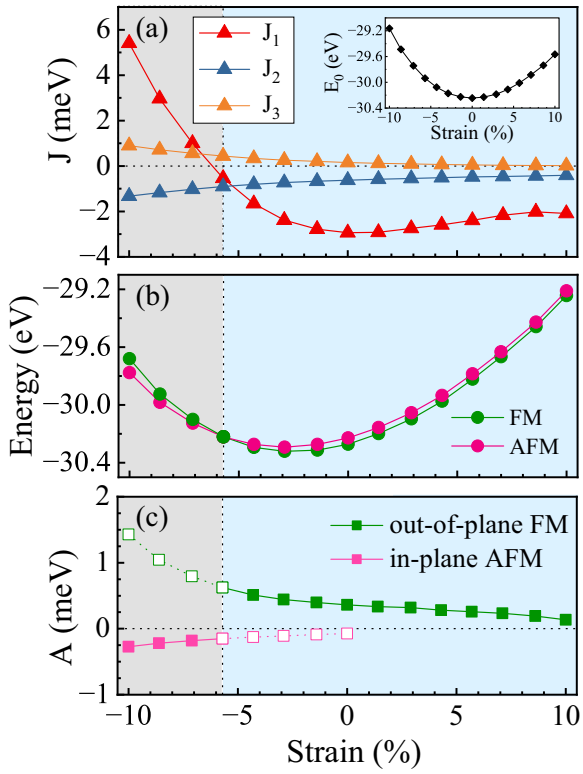

FIG. 2. Calculated Heisenberg exchange interaction parameters (a), total energies for different magnetic orders (b), and single-ion anisotropy parameter A (c) as a function of biaxial strain. Inset: calculated nonmagnetic energy E_0 as a function of strain. The error bars are smaller than the symbol size. The gray and blue shading indicates corresponding ferromanetic and anti-ferromagnetic ground states, respectively, determined by the total energies.

range under discussion. The results agree well with those reported in Ref. [28]. The above calculations are carried out without taking relativistic effects into account, which have been proven to have negligible effects on isotropic exchange interactions [28].

The sign change of the dominant exchange interaction results from competition between positive direct exchange that favors AFM order and negative superexchange that favors the FM configuration. The former remarkably increases as the compressive strain increases, while the latter is less sensitive to lattice compression. This suggests that the ground state can change from FM to AFM as a larger compressive strain is applied. We confirm this by calculating the total energies, in this case with relativistic effects taken into account, of an FM state and an AFM state at different strain values, as shown in Fig. 2(b). With a compressive strain larger (in magnitude) than -5.7%, the lower energy of the AFM state indicates that it is the ground state rather than the FM state.

We further determine the single-ion magnetic anisotropy parameter A by calculating the energy difference between states with magnetizations in-plane and out-of-plane: $E_{\parallel} - E_{\perp} = AS^2$. Combining with the magnetic order in the ground state determined from the total energy calculations, we obtain A for FM and AFM states, respectively. The results are plotted in Fig. 2(c). The value at zero strain corresponds to a magnetic anisotropy energy of 0.82 meV per Cr atom, which is consistent with previous results, ranging from 0.65 to 0.98 meV [18,51,66,69]. Positive (negative) A indicates out-of-plane (in-plane) magnetization at ground state. The empty squares show continuous tendencies if magnetic order is unchanged as being FM (green) and AFM (pink), respectively. The discontinuity of the solid curve occurs at the compressive strain -5.7% where the magnetic phase transition takes place.

III. NONLINEAR SPIN-WAVE THEORY

For a magnon system with isotropic Heisenberg exchange interactions and single-ion magnetic anisotropy, the magnon Hamiltonian is usually given as

$$H = \sum_{\langle ij \rangle} J_{ij} \mathbf{S}_i \cdot \mathbf{S}_j - |A| \sum_i \left(S_i^{\xi}\right)^2, \tag{2}$$

where $\langle ij \rangle$ represents the summation over neighbor pairs with corresponding exchange coefficients J_{ij} and ξ is the direction of the easy axis. The anisotropic exchange and the Dzyloshinskii-Moriya interaction arising from spin-orbit interaction are not taken into account, which may yield small gaps in magnon spectra and/or topological properties of magnons in CrI_3 [70,71]. These variations are nevertheless in a much smaller energy scale than the influence of magnon-magnon interaction at finite temperature that we study in this work.

A. Honeycomb ferromagnets

For FM single-layer CrI_3, there are two magnetic sublattices, Cr_A and Cr_B, as shown in Fig. 1, with spins parallel and out-of-plane. Using the Holstein-Primakoff transformation [72], one extends LSWT to NLSWT by including quartic terms and truncating higher-order terms:

$$\begin{aligned} S_A^+ &= (\sqrt{2S - a^+ a})a \approx \sqrt{2S}\left(a - \frac{a^\dagger a a}{4S}\right), \\ S_A^- &= a^\dagger(\sqrt{2S - a^+ a}) \approx \sqrt{2S}\left(a^\dagger - \frac{a^\dagger a a}{4S}\right), \\ S_A^z &= S - a^+ a, \end{aligned} \tag{3}$$

where $a^\dagger$ and a are the creation and annihilation operators of magnons, respectively, for sublattice Cr_A, and $S = 3/2$ is the magnitude of the atomic spin. Substituting $a^\dagger(a)$ with $b^\dagger(b)$ in the above equations, we obtain the expressions for sublattice Cr_B. With $S^{\pm} = S^x \pm iS^y$ and $\xi = z$ in Eq. (2) and standard Fourier transforms

$$d_i^\dagger = \frac{1}{\sqrt{N}} \sum_{\mathbf{k}} e^{-i\mathbf{k}\cdot\mathbf{R_i}} d_{\mathbf{k}}^\dagger, \quad d_i = \frac{1}{\sqrt{N}} \sum_{\mathbf{k}} e^{i\mathbf{k}\cdot\mathbf{R_i}} d_{\mathbf{k}}, \tag{4}$$

where $d = a, b$, we deduce the magnon Hamiltonian using operators $a_{\mathbf{k}}$ ($a_{\mathbf{k}}^\dagger$) and $b_{\mathbf{k}}$ ($b_{\mathbf{k}}^\dagger$) in k space. The four-operator terms are treated within the mean-field approximation and reduced to two-operator terms (the detailed derivation can be found in Appendix A), and the magnon Hamiltonian is obtained as

$$\mathrm{H_{FM}} = \sum_{\mathbf{k}} (a_{\mathbf{k}}^\dagger \; b_{\mathbf{k}}^\dagger) \begin{pmatrix} \mathcal{A}(\mathbf{k}) & \mathcal{B}(\mathbf{k}) \\ \mathcal{B}^*(\mathbf{k}) & \mathcal{A}(\mathbf{k}) \end{pmatrix} \begin{pmatrix} a_{\mathbf{k}} \\ b_{\mathbf{k}} \end{pmatrix}, \tag{5}$$

where $\mathcal{A}(\mathbf{k})$ and $\mathcal{B}(\mathbf{k})$ contain contributions from both magnon noninteracting and interacting terms:

$$\begin{aligned}\mathcal{A}(\mathbf{k}) &= -\sum_{\rho=1}^{3} J_\rho Z_\rho [M + \mathrm{Re}(f_\rho)] + J_2 Z_2 \gamma_2(k)(M + f_2) \\ &\quad - (2S + 1 - 4M)A, \\ \mathcal{B}(\mathbf{k}) &= \sum_{\rho=1,3} J_\rho Z_\rho (M + f_\rho)\gamma_\rho(k). \end{aligned} \tag{6}$$

Here Z_ρ is the number of neighbor pairs ($Z_1 = 3$ for the nearest, $Z_2 = 6$ for the second-nearest, and $Z_3 = 3$ for the third-nearest neighbors), $\gamma_\rho(k)$ is the structural factor determined by the lattice,

$$\begin{aligned}\gamma_1(k) &= \frac{1}{3}\Bigg[\cos\left(\frac{a_0}{\sqrt{3}}k_y\right) + 2\cos\left(\frac{a_0}{2}k_x\right)\cos\left(\frac{a_0}{2\sqrt{3}}k_y\right) \\ &\quad + i\left(\sin\left(\frac{a_0}{\sqrt{3}}k_y\right) - 2\cos\left(\frac{a_0}{2}k_x\right)\sin\left(\frac{a_0}{2\sqrt{3}}k_y\right)\right)\Bigg], \\ \gamma_2(k) &= \frac{1}{3}\left(\cos(a_0 k_x) + 2\cos\left(\frac{a_0}{2}k_x\right)\cos\left(\frac{\sqrt{3}a_0}{2}k_y\right)\right), \\ \gamma_3(k) &= \frac{1}{3}\Bigg[\cos\left(\frac{2a_0}{\sqrt{3}}k_y\right) + 2\cos(a_0 k_x)\cos\left(\frac{a_0}{\sqrt{3}}k_y\right) \\ &\quad + i\left(-\sin\left(\frac{2a_0}{\sqrt{3}}k_y\right) + 2\cos(a_0 k_x)\sin\left(\frac{a_0}{\sqrt{3}}k_y\right)\right)\Bigg], \end{aligned} \tag{7}$$

and we have the following:

$$M = S - \frac{1}{N}\sum_k \langle a_k^\dagger a_k\rangle, \tag{8}$$

$$f_\rho = \frac{1}{N}\sum_k \gamma_\rho(-k)\langle b_k^\dagger a_k\rangle \quad (\rho = 1, 3), \tag{9}$$

$$f_2 = \frac{1}{N}\sum_k \gamma_2(k)\langle a_k^\dagger a_k\rangle. \tag{10}$$

In the above three expressions, $\langle \dots \rangle$ means the mean-field treatment. We also have $S = 3/2$ for the atomic spin, a_0 for the lattice constant, and N for the number of k points, which is checked to be well converged. The magnetization M given in Eq. (8) is the same for both sublattices. The short-range bosonic correlations within one sublattice and between different sublattices are characterized by f_2 in Eq. (10) and f_1 and f_3 in Eq. (9), respectively. The latter correlations result in coherent superimposition of magnon modes from different sublattices. Through canonical transformation, the diagonalized Hamiltonian is obtained as

$$H_k = \sum_k E_+ \alpha_{\mathbf{k}}^\dagger \alpha_{\mathbf{k}} + E_- \beta_{\mathbf{k}}^\dagger \beta_{\mathbf{k}}, \tag{11}$$

where the eigenvalues read

$$E_\pm(\mathbf{k}) = \mathcal{A}(\mathbf{k}) \pm |\mathcal{B}(\mathbf{k})|, \tag{12}$$

and the noninteracting bosonic quasiparticle operators α_k and β_k are determined by interacting bosons a_k and b_k as

$$\begin{pmatrix}\alpha_{\mathbf{k}} \\ \beta_{\mathbf{k}}\end{pmatrix} = \frac{1}{\sqrt{2}}\begin{pmatrix}1 & e^{i\phi_{\mathbf{k}}} \\ -e^{-i\phi_{\mathbf{k}}} & 1\end{pmatrix}\begin{pmatrix}a_{\mathbf{k}} \\ b_{\mathbf{k}}\end{pmatrix}, \tag{13}$$

with the phase being $\phi_{\mathbf{k}} = \arg[\mathcal{B}(\mathbf{k})]$. With the above expressions, we rewrite Eqs. (8)–(10) as

$$M = S - \frac{1}{2N}\sum_{k,\sigma=\pm} n_\sigma(k), \tag{14}$$

$$f_\rho = \frac{1}{2N}\sum_{k,\sigma=\pm} \sigma\gamma_\rho(-k)e^{i\phi_{\mathbf{k}}} n_\sigma(k) \quad (\rho = 1, 3), \tag{15}$$

$$f_2 = \frac{1}{2N}\sum_{k,\sigma=\pm} \gamma_2(k) n_\sigma(k), \tag{16}$$

where $n_\pm(k) = 1/(e^{\beta E_\pm(k)} - 1)$, and $\beta = 1/k_B T$ introduces thermal effects into the magnon system through the Bose-Einstein distribution. By self-consistently solving Eqs. (6)–(7), (12), and (14)–(16), we obtain (1) the magnon spectrum $E_\pm(\mathbf{k})$ for the acoustic and optical branches at zero temperature and (2) the magnetic thermodynamic properties at a finite temperature, which will be further detailed in Sec. IV B.

B. Honeycomb antiferromagnets

In AFM single-layer CrI_3, spins on different sublattices are antiparallelly aligned in the x-y plane. Assuming that the spins are along the x direction, we have for sublattice Cr_A the same as Eq. (3) (substituting S_A^z with S_A^x), but for sublattice Cr_B,

$$\begin{aligned} S_B^+ &= b^\dagger(\sqrt{2S - b^+ b}) \approx \sqrt{2S}\left(b^\dagger - \frac{b^\dagger b b}{4S}\right), \\ S_B^- &= (\sqrt{2S - b^+ b})b \approx \sqrt{2S}\left(b - \frac{b^\dagger b b}{4S}\right), \\ S_B^x &= b^+ b - S. \end{aligned} \tag{17}$$

Here, with $S^\pm = S^y \pm iS^z$ and $\xi = x$ in Eq. (2) and the same Fourier transforms as in Eq. (4), we obtain the AFM magnon Hamiltonian as (derivation details are given in Appendix A)

$$H_{\mathrm{AFM}} = \sum_{\mathbf{k}} (a_{\mathbf{k}}^\dagger \;\; b_{-\mathbf{k}})\begin{pmatrix}\tilde{\mathcal{A}}(\mathbf{k}) & \tilde{\mathcal{B}}(\mathbf{k}) \\ \tilde{\mathcal{B}}^*(\mathbf{k}) & \tilde{\mathcal{A}}(\mathbf{k})\end{pmatrix}\begin{pmatrix}a_{\mathbf{k}} \\ b_{-\mathbf{k}}^\dagger\end{pmatrix}, \tag{18}$$

where

$$\begin{aligned}\tilde{\mathcal{A}}(\mathbf{k}) &= \sum_{\rho=1,3} J_\rho Z_\rho (M - Re[f_\rho]) + J_2 Z_2(\gamma_2(k) - 1) \\ &\quad \times (f_2 + M) - (2S - 4M + 1)A, \\ \tilde{\mathcal{B}}(\mathbf{k}) &= \sum_{\rho=1,3} J_\rho Z_\rho \gamma_\rho(k)(M - f_\rho), \end{aligned} \tag{19}$$

with Z_ρ and γ_ρ given previously in Sec. III A and

$$M = S - \frac{1}{N}\sum_k \langle a_k^\dagger a_k\rangle, \tag{20}$$

$$f_\rho = \frac{1}{N}\sum_k \gamma_\rho(-k)\langle a_k b_{-k}\rangle \quad (\rho = 1, 3), \tag{21}$$

$$f_2 = \frac{1}{N}\sum_k \gamma_2(k)\langle a_k^\dagger a_k\rangle. \tag{22}$$

We diagonalize the Hamiltonian by applying the Bogoliubov-Valatin canonical transformation [73] as $U^\dagger H_{\mathrm{AFM}} U = H_k$,

where the transformation matrix reads

$$U = \frac{1}{\sqrt{2E_k[\tilde{\mathcal{A}}(\mathbf{k}) - E_k]}} \begin{pmatrix} \tilde{\mathcal{B}}(\mathbf{k}) & E_k - \tilde{\mathcal{A}}(\mathbf{k}) \\ E_k - \tilde{\mathcal{A}}(\mathbf{k}) & \tilde{\mathcal{B}}^*(\mathbf{k}) \end{pmatrix}. \tag{23}$$

It also satisfies $U^\dagger \sigma_z U = \sigma_z$, with $\sigma_z = \mathrm{diag}(1, -1)$. The diagonal eigenvalue matrix is

$$H_k = \sum_k E_k(\alpha_{\mathbf{k}}^\dagger \alpha_{\mathbf{k}} + \beta_{\mathbf{k}}^\dagger \beta_{\mathbf{k}}), \tag{24}$$

where the new annihilation (creation) operators $\alpha_k(\beta_{-k}^\dagger)$ are introduced as

$$\begin{pmatrix} \alpha_{\mathbf{k}} \\ \beta_{-\mathbf{k}}^\dagger \end{pmatrix} = U^{-1} \begin{pmatrix} a_{\mathbf{k}} \\ b_{-\mathbf{k}}^\dagger \end{pmatrix}, \tag{25}$$

and the excitation spectrum is

$$E_k = \sqrt{[\tilde{\mathcal{A}}(\mathbf{k})]^2 - |\tilde{\mathcal{B}}(\mathbf{k})|^2}. \tag{26}$$

Without an external magnetic field, the excitation spectrum is degenerate. The Bose distribution satisfies $n_k = 1/(e^{\beta E_k} - 1)$. We further rewrite Eqs. (20)–(22) as

$$M = S - \frac{1}{N} \sum_{\mathbf{k}} \frac{(2n_k + 1)\tilde{\mathcal{A}}(\mathbf{k}) - E_k}{2E_k}, \tag{27}$$

$$f_\rho = -\frac{1}{N} \sum_{\mathbf{k}} \gamma_\rho(-k) \frac{(2n_k + 1)\tilde{\mathcal{B}}(\mathbf{k})}{2E_k} \quad (\rho = 1, 3), \tag{28}$$

$$f_2 = \frac{1}{N} \sum_{\mathbf{k}} \gamma_2(k) \frac{(2n_k + 1)\tilde{\mathcal{A}}(\mathbf{k}) - E_k}{2E_k}. \tag{29}$$

By self-consistently solving Eqs. (7), (19), and (26)–(29), we obtain the AFM magnon spectrum and the related properties.

IV. RESULTS AND DISCUSSION

Iteratively solving the above NLSWT formalism with the numerical values of the exchange interactions J_1, J_2, and J_3 and the single-ion anisotropy A calculated from first principles in Fig. 2, we obtain magnetic properties for the FM and AFM states. At zero temperature, the results from the NLSWT formalism are the same as those from LSWT [74]. With increasing the temperature, lattice vibration is excited, which thermalizes the spin system via the magnon-phonon interaction [74]. In this section, we focus on the magnon-magnon interaction and study its influence on finite-temperature magnetism using the NLSWT.

A. Zero temperature

At $T = 0$ K, the magnon spectra for FM and AFM states are obtained as in Eqs. (12) and (26), respectively. The results are shown in Fig. 3, with the high-symmetry path of the honeycomb lattice marked in Fig. 1(d). In the case of the FM state, increasing tensile strain leads to softening of the magnon excitation energy, as shown in Fig. 3(a), consistent with the decreasing exchange coupling and single-ion anisotropy shown in Fig. 2. With increasing compressive strain, the magnon spectra in Fig. 3(b) significantly decrease, originating mainly from the decreasing exchange interaction J_1 between

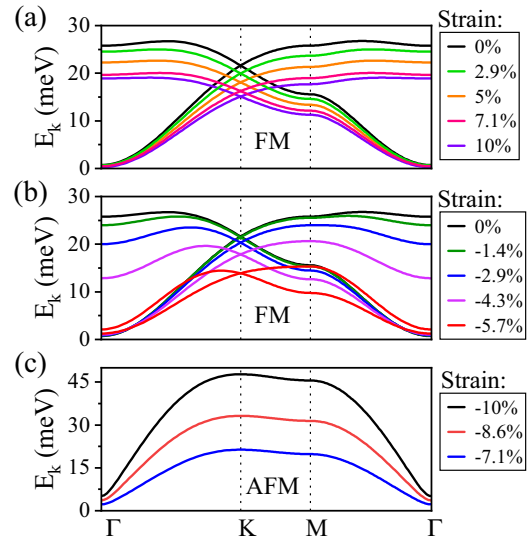

FIG. 3. Spin-wave excitation spectra for ferromagnetic and antiferromagnetic single-layer CrI_3 at zero temperature, calculated based on the DFT results of the exchange interaction and single-ion anisotropy with respect to different lattice strain values. Positive strain stands for tension (a), and negative strain stands for compression [(b),(c)].

nearest neighbors. At a strain of −5.7%, the ground state changes from FM to AFM, and the optical branch becomes very close to the acoustic branch, approaching a degenerate AFM spectrum, as shown in Fig. 3(c). With an even larger compressive strain, the AFM spectra substantially increase, determined by the rapidly increasing J_1, as shown in Fig. 2(a).

A closer inspection of the spectra at the Γ point shows the energy of the acoustic branch at $k = 0$, usually called the energy gap and denoted Δ. It determines the stability of the 2D magnetism, decreases with increasing tensile strain, as shown in Fig. 3(a), and increases with increasing compressive strain, as shown in Fig. 3(b), consistent with the monotonic variation of the single-ion magnetic anisotropy A with the lattice strain in the FM state, as shown in Fig. 2(b). According to the NLSWT formalism, we have $\Delta = \mathcal{A}(0) + |\mathcal{B}(0)|$, as given in Eq. (12). Plugging the structural factors $\gamma = 1$ for the Γ point given in Eq. (7) into Eq. (6), we have $\Delta = A(4M - 2S - 1)$. At $T = 0$ K, the atomic magnetization given in Eq. (14) is $M = S$. We thus have the energy gap $A(2S - 1)$ determined only by the single-ion magnetic anisotropy.

For the AFM state, we first determine the magnon spectra for various lattice strain values, as shown in Fig. 3(c). $\Delta = E_{k=0}$ remarkably increases with compressive strain. Although our NLSWT formalism does not give an analytical expression for it, one finds its positive correlation with the single-ion magnetic anisotropy, as intuitively expected.

B. Finite temperatures

With the temperature introduced through the Bose distribution, we calculate the magnetic properties with a temperature dependence for FM and AFM single-layer CrI_3 by self-consistently solving the corresponding equations listed above. The critical Curie temperature, T_C, for the FM state and Néel

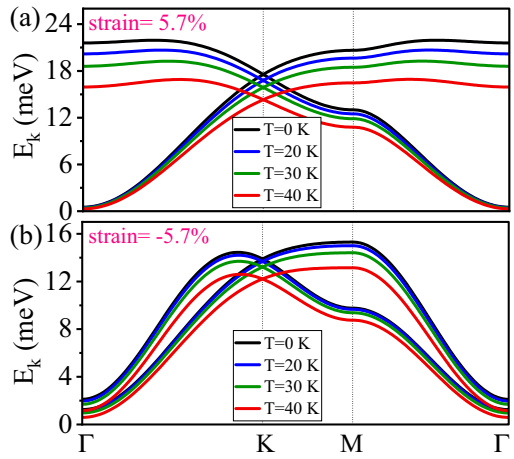

FIG. 4. Calculated magnon spectra for ferromagnetic single-layer CrI_3 at a tensile strain of 5.7% (a) and a compressive strain of −5.7% (b) at different temperatures below their Curie temperatures.

temperature, T_N, for the AFM state are determined at vanishing magnetization [75].

1. Ferromagnetic

In the FM case, we calculate the magnon spectra at different temperatures for various lattice strains. Taking the tensile strain of 5.7% and compressive strain of −5.7% as examples, we show magnon spectra softening with increasing temperature, as plotted in Fig. 4. With a tensile strain of 5.7%, both the acoustic and optical branches become lower in energy, with the latter change appearing more remarkable. At a compressive strain of −5.7%, the two branches are close to each other at relatively low energies (compared to those at a tensile strain of 5.7%), and both soften by only a couple of meV.

We can further determine the energy gap Δ at the Γ point for different temperature and strain values. The results are plotted in Fig. 5. A monotonic decrease with temperature applies to all FM states with various lattice strains as shown in Fig. 5(a). This means that the stability of the 2D ferromagnetism decreases as the temperature increases, as intuitively

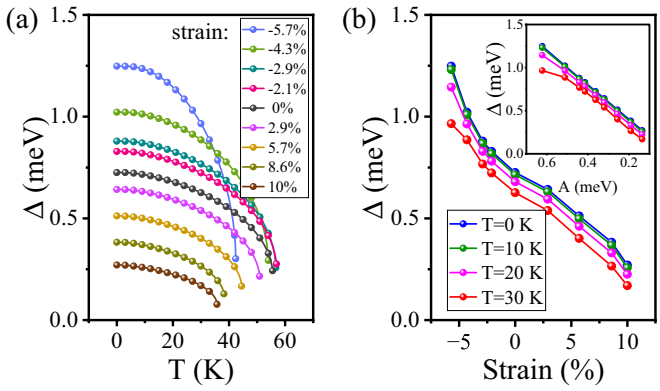

FIG. 5. Calculated energy gap of the acoustic branch of the magnon spectra at the Γ point for FM single-layer CrI_3 as a function of temperature (a) and lattice strain (b). Inset: Calculated energy gap as a function of the single-ion magnetic anisotropy.

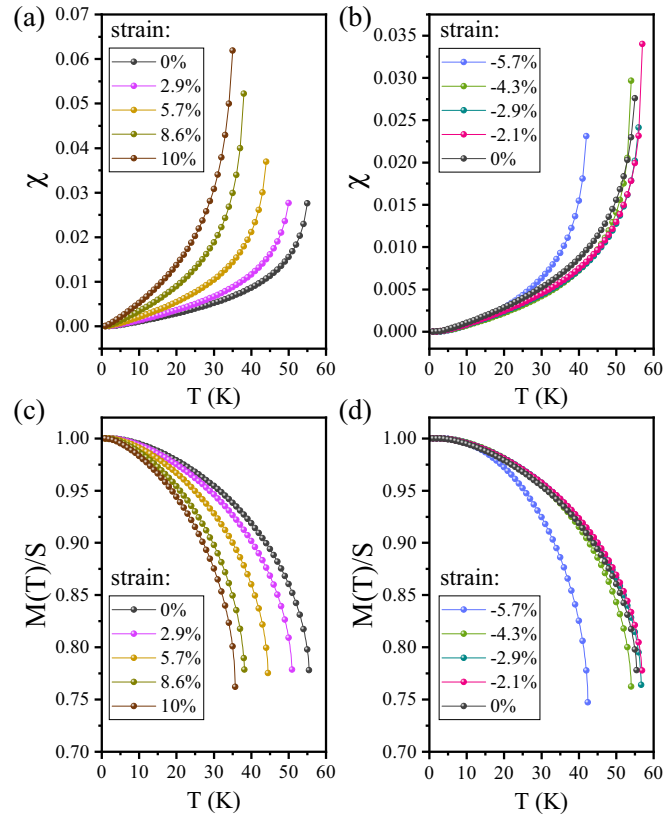

FIG. 6. Calculated static susceptibility [(a),(b)] and reduced spontaneous magnetization [(c),(d)] as a function of temperature at various lattice strains.

expected. This is thus equivalent to determining the critical temperature at $\Delta = 0$ [75]. Close to the FM-AFM transition, the compressive strain of −5.7% leads to an extraordinarily small T_C. By replotting the energy gap as a function of lattice strain, as shown in Fig. 5(b), we obtain a monotonic decrease. As discussed in Sec. IV A, Δ is mainly determined by the single-ion magnetic anisotropy A. Plotting Δ as a function of A, as shown in the inset in Fig. 5(b), we find a linear dependence at low temperatures and a deviation from linear becoming noticeable with increasing temperature. This confirms that the energy gap, which supports the long-range magnetic order surviving thermal fluctuations, is determined by the magnetic anisotropy.

Based on the temperature-dependent magnon spectra, we calculate the static susceptibility, which is defined as [76]

$$\chi = \frac{1}{2NT} \sum_{\mathbf{k},\sigma=\pm} \frac{\exp\left[E_{\mathbf{k}\sigma}(T)/k_B T\right]}{\left\{\exp\left[E_{\mathbf{k}\sigma}(T)/k_B T\right]-1\right\}^2} \tag{30}$$

and plot the results in Figs. 6(a) and 6(b). The susceptibility increases with increasing temperature and diverges at the Curie temperature. Larger tensile strains give rise to faster divergence, as shown in Fig. 6(a), while compressive strains, as shown in Fig. 6(b), except for the critical strain of −5.7% where the system is close to the FM-AFM phase transition, show little effect on the diverging tendency.

Similar behaviors are found in the reduced spontaneous magnetization, which is plotted as a function of temperature

at various lattice strains in Figs. 6(c) and 6(d). At zero temperature, the reduced magnetization is unity, and spins are fully out-of-plane in the FM ground state. With increasing temperature, the excitation of magnons, $n(k)$ given in Eq. (14), increases, resulting in a decreasing M. With tensile strains, as shown in Fig. 6(c), larger strain values lead to a faster decrease in $M(T)$. In contrast, compressive strains show a weak influence on the reduction of $M(T)$, as shown in Fig. 6(d), except for the strain of -5.7%. By further fitting the magnetization using the expression [77] $M(T)/S = 1 - (T/T_C)^{\alpha}$ in the low-temperature region, we find that the index α is systematically larger than 3/2. Specifically, it is approximately 2 for all the tensile and compressive strains (except for the strain of -5.7%, where it is approximately 2.6) and increases as the lattice becomes smaller. We therefore demonstrate that the Bloch $T^{3/2}$ law does not hold for the 2D CrI_3 system.

2. Antiferromagnetic

With a compressive strain larger than -5.7%, single-layer CrI_3 is in the ground state of an in-plane antiferromagnet. The temperature-dependent magnon spectra are self-consistently calculated, as discussed in Sec. III B. Taking the compressive strain of -8.6% as an example, we plot the results in Fig. 7(a). The magnon excitation energy decreases as the temperature increases, similar to the case of the FM state (shown in Fig. 4). However, this softening of the magnon spectra is much less remarkable in Fig. 7(a) than in Fig. 4. Quantitatively, the softening of the AFM magnon at the K point is approximately several percent when approaching the critical Néel temperature, while the softening of the FM optical branch at the Γ point in Fig. 4 is close to half around T_C.

The corresponding energy gap Δ as a function of temperature is shown in Fig. 7(b). Again, a monotonic decrease is found, which indicates that the stability of the AFM state also weakens with increasing temperature, as intuitively expected. Nevertheless, with a much larger Δ at 0 K, the AFM long-range order holds until a much higher temperature compared to the FM case. Meanwhile, the (quasi-)linear dispersion of the magnon spectra in the AFM state results in a relatively small density of states (DOS) of excited magnon modes. The population of magnons with increasing temperature is thus restricted by such a low DOS. In contrast, the FM state with a (quasi-)quadratic dispersion in the low-energy region leads to a larger DOS and, in turn, a larger magnon population with increasing temperature. The magnon-magnon interaction, which is accounted for in NLSWT, is therefore stronger in the FM case than in the AFM state.

We can obtain deeper insight into the magnon-magnon interaction by examining the atomic magnetization as a function of temperature in the AFM state, as shown in Fig. 7(c). The magnitudes of the reduced magnetization of the two sublattices in the AFM single-layer CrI_3 are the same, and they both decay with increasing temperature, similar to the case of the FM state shown in Figs. 6(c) and 6(d). With increasing compressive strain, the dominant exchange interaction and single-ion anisotropy both increase (Fig. 2). The stability of the AFM state is thus enhanced, which manifests as an increasing critical Néel temperature. Meanwhile, there are two aspects attractively distinct from the FM case: (1) $M(T)$ decays much faster than in the FM case and (2) the reduced magnetization at 0 K is less than unity.

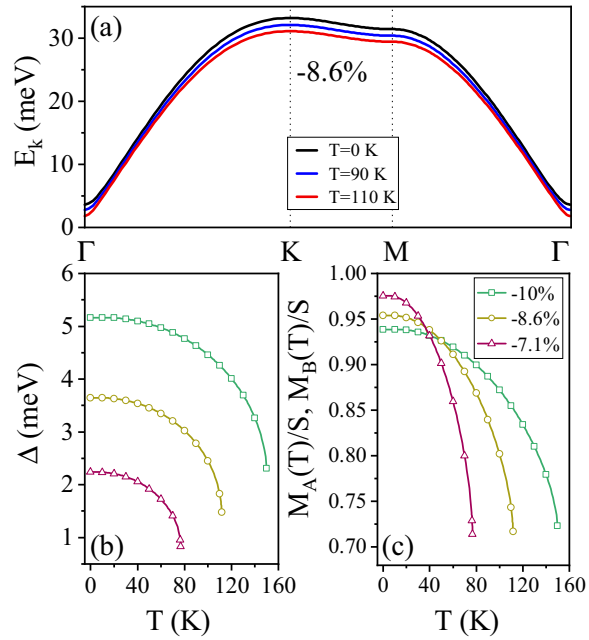

FIG. 7. (a) Calculated magnon spectra for antiferromagnetic single-layer CrI_3 at a compressive strain of -8.6% at different temperatures below the critical Néel temperature. Calculated energy gap of the magnon spectra (b) and atomic magnetization of two sublattices in antiferromagnetic CrI_3 (c) as a function of temperature at various lattice strain values.

Provided that the relation $1 - (T/T_C)^{\alpha}$ also holds for the AFM case, we fit the atomic magnetization here and obtain α values close to 3 for these three compressive strains, which are much larger than the α values in the FM case. This again confirms the weak excitation of AFM magnons and therefore the weak magnon-magnon interaction leading to negligible softening of the magnon spectra.

We replot the reduced magnetization at 0 K in Fig. 8 using solid symbols and find a mild decrease with increasing compressive strength, but the values are systematically smaller than 1. The latter means that the atomic spins are not fully parallel within one sublattice, and this is well known in AFM system, as fluctuations of spins lower the total energy [56]. However, by artificially resetting the value of the single-ion anisotropy A, as shown by the dashed lines, we show a unity reduced magnetization, as in the FM case, if A is infinitely large and a further diminished (but only by a couple of percent) magnetization if $A = 0$. This means that large anisotropy suppresses spin fluctuations and favors parallel alignment of spins within one sublattice. The dependence of the reduced magnetization at 0 K on the strain values is introduced through exchange interactions.

3. Critical temperature

The critical Curie and Néel temperatures of 2D single-layer CrI_3 are determined at vanishing magnetization of each sublattice (or equivalently at vanishing energy gap, $\Delta = 0$)

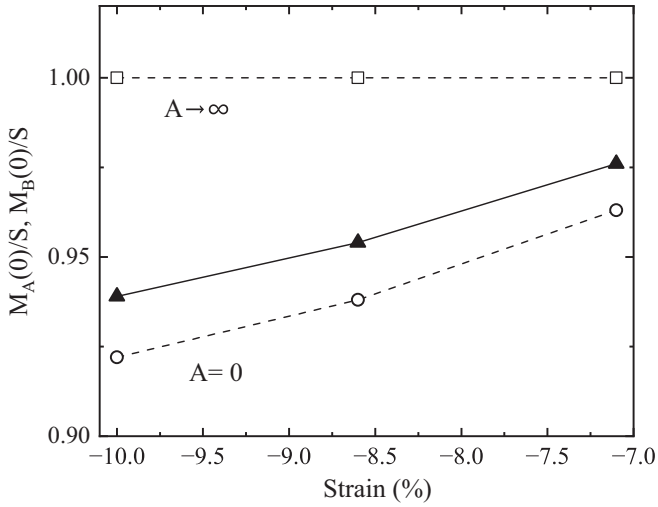

FIG. 8. Calculated atomic magnetization of two sublattices at zero temperature as a function of compressive strain in the AFM state.

[75] for the FM and AFM states, respectively. We plot the results in Fig. 9 using solid symbols. In the FM state, the Curie temperature shows a nonmonotonic dependence on the strain, similar to the behavior of the dominant exchange interaction between nearest neighbors, J_1, shown in Fig. 2. Combined with the monotonic J_2, J_3, and A, the maximum value of $T_C = 57$ K appears at a compressive strain of -2.1%. A much larger decay occurs when further compressing the lattice than when stretching it. For the original lattice size, 0% strain, we obtain $T_C = 55.5$ K, which is larger than the measured value 45 K [2], as marked by the star in Fig. 9. The same situation was found for $Cr_2Ge_2Te_6$ [1], where the calculated exchange interaction J and single-ion magnetic anisotropy A were plugged into NLSWT and an overestimated T_C was obtained.

Nevertheless, there are also theoretical studies of single-layer CrI_3 that reported T_C in better agreement with experiments [18,45,75,78], as marked in Fig. 9. We find that in most

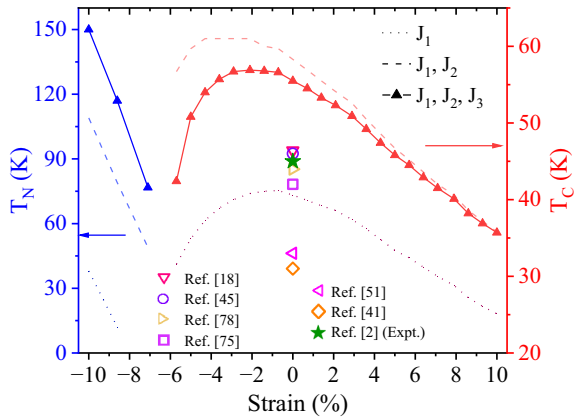

FIG. 9. Néel temperature (left) and Curie temperature (right) as a function of lattice strain. The experimental value [2] is marked using a solid star. The open symbols mark theoretical results [18,41,45,51,75,78] from the literature.

of these studies [18,45,75], as well as other studies that gave even smaller T_C [41,51], only the nearest-neighbor exchange interaction was considered in the simulations. We carry out a similar treatment (details can be found in Appendix B), in which we also ignore the next-nearest-neighbor exchange interaction J_2 and the third-nearest-neighbor exchange interaction J_3 and attribute their contributions to J_1. This effective J_1 leads to a systematically smaller T_C, as plotted by the dotted curve in Fig. 9. Better agreement with experiments is thus found here. We further include J_2 and ignore only J_3. The effective J_1 and J_2 give an obviously overestimated T_C, as plotted by the dashed curve. This indicates that J_2, although small, plays an important role in determining the stability of the magnetism in single-layer CrI_3. Ignoring it leads to substantial underestimation of T_C. The AFM exchange, $J_3 > 0$, slightly reduces T_C, as intuitively expected. Previous MC studies presented similar findings [37].

We therefore demonstrate that by changing the exchange interaction and single-ion magnetic anisotropy via lattice strain, one changes the T_C of single-layer CrI_3. There have been various approaches based on experimental measurements and theoretical calculations aiming at raising the Curie temperature of 2D magnetic materials, such as applying ionic gates [4], electrostatic doping [79], external magnetic fields [1,47,52], lattice strain [18,21,38], stacking [1,47,52], substitution of certain atoms with others [38], vacancies and interstitial atoms [80], and molecular absorption [81–83]. Effectively, they modify the exchange interaction and single-ion magnetic anisotropy by changing the electronic structure. NLSWT provides a straightforward method to estimate and/or predict the resulting effects on the Curie temperature once these parameters are determined during various investigations.

For the AFM configuration, the Néel temperature varies monotonically with strain, as shown by the blue solid line in Fig. 9. We also plot the results of calculations where fewer exchange interaction terms are taken into account, as shown by the dotted line (only J_1) and the dashed line (only J_1 and J_2). In the AFM ground state, spins are antiparallel among the nearest pairs and parallel among the next-nearest pairs. Considering the signs of the exchange coefficients, we have lower energy when including more exchange interaction terms and more stable AFM order. The Néel temperature therefore increases when more J terms are taken into account. This again confirms that only the nearest-neighbor exchange term is not sufficient to describe the magnetic state and related properties.

V. CONCLUSIONS

The magnetic properties of single-layer CrI_3 have been theoretically investigated with first-principles calculations and NLSWT combined. We confirmed the magnetic phase transition, from out-of-plane FM order to in-plane AFM order, at compressive lattice -5.7% found in previous studies as a benchmark. We further determined the exchange interactions between the nearest, next-nearest, and third-nearest neighbors, as well as the single-ion anisotropy, which protects the long-range magnetic order in this 2D system. Substituting these parameters into the NLSWT formalism for FM and AFM

states, we obtained, through self-consistent calculations, the magnon spectra both at zero and finite temperatures. The lowest excitation energy of the spectra, or the energy gap, protects the magnetism from breakdown according to the Mermin-Wagner theorem. It is found to decrease with increasing temperature, similar to the temperature-dependent atomic magnetization, both of which vanish at the critical Curie and Néel temperatures for FM and AFM magnetism, respectively. We showed that the magnetization of a given sublattice in the system decays from 1 to 0 with temperature in the FM state, while with finite anisotropy, it decays starting from less than 1 in the AFM state. We further demonstrated that the critical temperatures would be significantly underestimated if only the nearest-neighbor exchange interaction was taken into account. With three exchange interaction coefficients, we obtained the Curie temperature of the intact single-layer CrI_3 lattice, although it was larger than the experimental value (this overestimation was also found in other 2D systems), and we suggest that this treatment is more physically reasonable.

ACKNOWLEDGMENTS

The authors are grateful for the helpful discussion with Ka Shen. Financial support for this study was provided by the National Natural Science Foundation of China (Grants No. 12374101, No. 11734004, and No. 12174028).

APPENDIX A: DETAILS OF DERIVATIONS

The magnon Hamiltonian, as in Eq. (2), is written in real space with a summation over atomic spins. With the spins expressed in terms of the creation and annihilation operators of magnons, as given in Eqs. (3) and (17), as well as their Fourier transforms given in Eq. (4), the magnon Hamiltonian can be further deduced as a summation over $\mathbf{k}$ space with two-operator terms and four-operator terms. Below we give details about these terms and the mean-field treatment, which reduces the four-operator terms to two-operator terms for the FM and AFM order.

For FM single-layer CrI_3, Eqs. (2)–(4) lead to a Hamiltonian containing two parts: $H_{\mathrm{FM}} = H_2^{\mathrm{FM}} + H_4^{\mathrm{FM}}$. H_2^{FM} corresponds to the two-operator terms, or the quadratic terms, and H_4^{FM} corresponds to the four-operator terms, or the quartic terms [47]. The former is the noninteracting term, and the latter involves magnon-magnon interaction:

$$H_2^{\mathrm{FM}} = \sum_{\mathbf{k}} (a_{\mathbf{k}}^\dagger \;\; b_{\mathbf{k}}^\dagger) \begin{pmatrix} \mathcal{A}_0(\mathbf{k}) & \mathcal{B}_0(\mathbf{k}) \\ \mathcal{B}_0^*(\mathbf{k}) & \mathcal{A}_0(\mathbf{k}) \end{pmatrix} \begin{pmatrix} a_{\mathbf{k}} \\ b_{\mathbf{k}} \end{pmatrix}, \tag{A1}$$

where

$$\begin{aligned} \mathcal{A}_0(\mathbf{k}) &= -\sum_{\rho} J_\rho Z_\rho S + J_2 Z_2 S \gamma_2(k) + (2S-1)A, \\ \mathcal{B}_0(\mathbf{k}) &= \sum_{\rho=1,3} J_\rho Z_\rho S \gamma_\rho(k), \end{aligned} \tag{A2}$$

and

$$\begin{aligned} H_4^{\mathrm{FM}} = \sum_{k_i \rho=1,3} \frac{J_\rho Z_\rho}{4N} & [4\gamma_\rho(k_4-k_2) a_{k_1}^\dagger b_{k_2}^\dagger a_{k_3} b_{k_4} - \gamma_\rho(-k_4) b_{k_1}^\dagger b_{k_2}^\dagger b_{k_3} a_{k_4} - \gamma_\rho(-k_1) b_{k_1}^\dagger a_{k_2}^\dagger a_{k_3} a_{k_4} - \gamma_\rho(k_1) a_{k_1}^\dagger b_{k_2}^\dagger b_{k_3} b_{k_4} \\ & - \gamma_\rho(k_4) a_{k_1}^\dagger a_{k_2}^\dagger a_{k_3} b_{k_4}] \delta_{k_1+k_2,k_3+k_4} + \frac{J_2 Z_2}{8N} \sum_{k_i} [4\gamma_2(k_4-k_2) a_{k_1}^\dagger a_{k_2}^\dagger a_{k_3} a_{k_4} - \gamma_2(-k_4) a_{k_1}^\dagger a_{k_2}^\dagger a_{k_3} a_{k_4} \\ & - \gamma_2(-k_1) a_{k_1}^\dagger a_{k_2}^\dagger a_{k_3} a_{k_4} - \gamma_2(k_1) a_{k_1}^\dagger a_{k_2}^\dagger a_{k_3} a_{k_4} - \gamma_2(k_4) a_{k_1}^\dagger a_{k_2}^\dagger a_{k_3} a_{k_4} + a \leftrightarrow b] \delta_{k_1+k_2,k_3+k_4} \\ & - \frac{A}{N} \sum_{k_i} \left(a_{k_1}^\dagger a_{k_2}^\dagger a_{k_3} a_{k_4} + b_{k_1}^\dagger b_{k_2}^\dagger b_{k_3} b_{k_4} \right) \delta_{k_1+k_2,k_3+k_4}. \end{aligned} \tag{A3}$$

Properties such as J_ρ, Z_ρ, and γ_ρ ($\rho = 1, 2, 3$) are defined the same as in Sec. III A. The Hartree-Fock-like decoupling is further applied to the four-boson terms [47]:

$$\begin{aligned} a_{k_1}^\dagger b_{k_2}^\dagger a_{k_3} b_{k_4} \approx{}& \langle a_{k_1}^\dagger a_{k_3} \rangle b_{k_2}^\dagger b_{k_4} + \langle b_{k_2}^\dagger b_{k_4} \rangle a_{k_1}^\dagger a_{k_3} \\ & + \langle a_{k_1}^\dagger b_{k_4} \rangle b_{k_2}^\dagger a_{k_3} + \langle b_{k_2}^\dagger a_{k_3} \rangle a_{k_1}^\dagger b_{k_4}, \\ a_{k_1}^\dagger a_{k_2}^\dagger a_{k_3} a_{k_4} \approx{}& \langle a_{k_1}^\dagger a_{k_3} \rangle a_{k_2}^\dagger a_{k_4} + \langle a_{k_2}^\dagger a_{k_4} \rangle a_{k_1}^\dagger a_{k_3} \\ & + \langle a_{k_1}^\dagger a_{k_4} \rangle a_{k_2}^\dagger a_{k_3} + \langle a_{k_2}^\dagger a_{k_3} \rangle a_{k_1}^\dagger a_{k_4}, \end{aligned} \tag{A4}$$

where $\langle a_k^\dagger a_{k'} \rangle = \delta_{kk'} \langle a_k^\dagger a_k \rangle$ and $\langle a_k^\dagger b_{k'} \rangle = \delta_{kk'} \langle a_k^\dagger b_k \rangle$. On the right-hand side of the above equations, scalar terms that do not affect the spin-wave dynamics are neglected [47]. Within this mean-field approximation, the four-boson terms are reduced to two-boson terms. Incorporating them with those in H_2, we arrive at the final expression for the FM magnon Hamiltonian given in Eq. (5).

Similarly, applying Eqs. (2)–(4) to AFM single-layer CrI_3 gives the AFM magnon Hamiltonian $H_{\mathrm{AFM}} = H_2^{\mathrm{AFM}} + H_4^{\mathrm{AFM}}$, and the quadratic H_2^{AFM} and quartic H_4^{AFM} in momentum space are written as

$$H_2^{\mathrm{AFM}} = \sum_{\mathbf{k}} (a_{\mathbf{k}}^\dagger \;\; b_{-\mathbf{k}}) \begin{pmatrix} \tilde{\mathcal{A}}_0(\mathbf{k}) & \tilde{\mathcal{B}}_0(\mathbf{k}) \\ \tilde{\mathcal{B}}_0^*(\mathbf{k}) & \tilde{\mathcal{A}}_0(\mathbf{k}) \end{pmatrix} \begin{pmatrix} a_{\mathbf{k}} \\ b_{-\mathbf{k}}^\dagger \end{pmatrix}, \tag{A5}$$

where

$$\begin{aligned} \tilde{\mathcal{A}}_0(\mathbf{k}) &= \sum_{\rho=1,3} J_\rho Z_\rho S - J_2 Z_2 S (1 - \gamma_2(k)) + 2AS, \\ \tilde{\mathcal{B}}_0(\mathbf{k}) &= \sum_{\rho=1,3} J_\rho Z_\rho S \gamma_\rho(k), \end{aligned} \tag{A6}$$

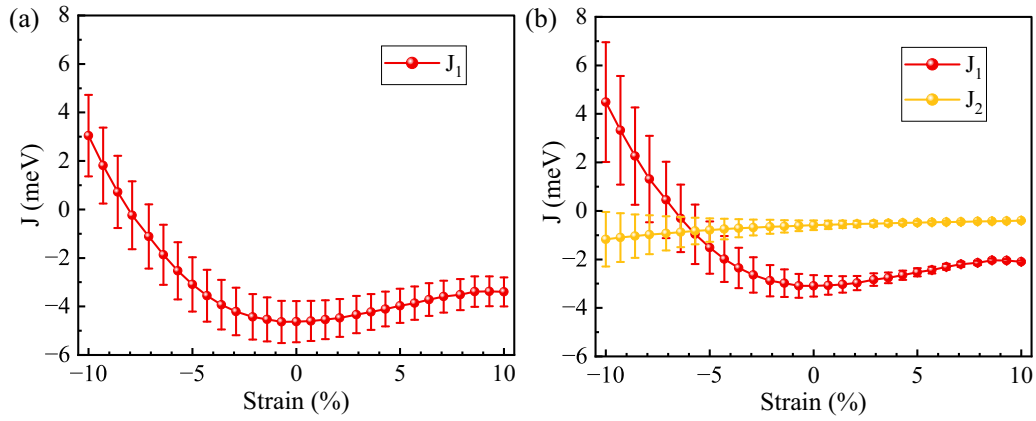

FIG. 10. Calculated Heisenberg exchange interaction parameters as a function of biaxial strain when only the nearest-neighbor interaction (a) and the next-nearest-neighbor interaction (b) are taken into account.

and

$$H_4^{\mathrm{AFM}} = -\sum_{k_i,\rho=1,3}\frac{J_\rho Z_\rho}{4N}\big[4\gamma_\rho(k_4-k_2)a^\dagger_{k_1}b^\dagger_{k_2}a_{k_3}b_{k_4}\delta_{k_1+k_2,k_3+k_4}+\gamma_\rho(-k_4)b^\dagger_{k_1}b_{k_2}b_{k_3}a_{k_4}\delta_{k_1,k_2+k_3+k_4}+\gamma_\rho(k_4)a^\dagger_{k_1}a_{k_2}a_{k_3}b_{k_4}\delta_{k_1,k_2+k_3+k_4}$$
$$+\gamma_\rho(k_1)a^\dagger_{k_1}b^\dagger_{k_2}b^\dagger_{k_3}b_{k_4}\delta_{k_1+k_2+k_3,k_4}+\gamma_\rho(-k_1)b^\dagger_{k_1}a^\dagger_{k_2}a^\dagger_{k_3}a_{k_4}\delta_{k_1+k_2+k_3,k_4}\big]+\frac{J_2Z_2}{4N}\sum_{k_i}\big[2\gamma_2(k_4-k_2)a^\dagger_{k_1}a^\dagger_{k_2}a_{k_3}a_{k_4}-(\gamma_2(k_1)$$
$$+\gamma_2(k_4))a^\dagger_{k_1}a^\dagger_{k_2}a_{k_3}a_{k_4}+a\leftrightarrow b\big]\delta_{k_1+k_2,k_3+k_4}-\frac{A}{N}\sum_{k_i}\big(a^\dagger_{k_1}a^\dagger_{k_2}a_{k_3}a_{k_4}+b^\dagger_{k_1}b^\dagger_{k_2}b_{k_3}b_{k_4}\big)\delta_{k_1+k_2,k_3+k_4}. \quad \text{(A7)}$$

A similar mean-field treatment is applied to the above H_4^{AFM}:

$$\begin{aligned}a^\dagger_{k_1}b^\dagger_{k_2}a_{k_3}b_{k_4} &\approx \langle a^\dagger_{k_1}a_{k_3}\rangle b^\dagger_{k_2}b_{k_4}+\langle b^\dagger_{k_2}b_{k_4}\rangle a^\dagger_{k_1}a_{k_3}\\ &\quad+\langle a^\dagger_{k_1}b^\dagger_{k_2}\rangle b_{k_3}a_{k_4}+\langle b_{k_3}a_{k_4}\rangle a^\dagger_{k_1}b^\dagger_{k_2},\\ a^\dagger_{k_1}a^\dagger_{k_2}a_{k_3}a_{k_4} &\approx \langle a^\dagger_{k_1}a_{k_3}\rangle a^\dagger_{k_2}a_{k_4}+\langle a^\dagger_{k_2}a_{k_4}\rangle a^\dagger_{k_1}a_{k_3}\\ &\quad+\langle a^\dagger_{k_1}a_{k_4}\rangle a^\dagger_{k_2}a_{k_3}+\langle a^\dagger_{k_2}a_{k_3}\rangle a^\dagger_{k_1}a_{k_4}, \quad \text{(A8)}\end{aligned}$$

where $\langle a^\dagger_k a_{k'}\rangle = \delta_{kk'}\langle a^\dagger_k a_k\rangle$ and $\langle a_k b_{k'}\rangle = \delta_{k,-k'}\langle a_k b_{-k}\rangle$. Incorporating H_2^{AFM} and H_4^{AFM} gives the expression of the AFM magnon Hamiltonian given in Eq. (18).

APPENDIX B: EFFECTS OF J_2 AND J_3

When mapping the total energies of the single-layer CrI_3 of 11 different collinear spin configurations, one can take into account various exchange interactions. As usually seen in the literature, it is common to attribute the energy to only the nearest-neighbor exchange term [18,41,45,51,75]. This means that only J_1 is considered in Eq. (1). In this manner, we carry out linear regression of the calculated total energies and determine J_1. Plotting the results in Fig. 10(a), we find similar behavior as the J_1 in Fig. 2, but with significantly large error bars. Analogously, we further include the next-nearest-neighbor exchange interaction, and we have J_1 and J_2 in Eq. (1). The same regression of these total energies yields both of these parameters. We plot them in Fig. 10(b) and find larger values and larger error bars at large compressive strains. Compared to the results in Fig. 2, where J_1, J_2, and J_3 are all taken into account, we show that the presence of J_3, although with very small values, plays an important role in reducing the error bars of the calculated results. At a large tensile strain, the error bars in Fig. 10(b) are as small as those in Fig. 2, and the vanishing J_3 in this region again confirms its importance. Physically, this means that the more exchange interaction terms are included, the more reasonable the description of the system is.

[1] C. Gong, L. Li, Z. Li, H. Ji, A. Stern, Y. Xia, T. Cao, W. Bao, C. Wang, Y. Wang *et al.*, Discovery of intrinsic ferromagnetism in two-dimensional van der Waals crystals, Nature (London) **546**, 265 (2017).

[2] B. Huang, G. Clark, E. Navarro-Moratalla, D. R. Klein, R. Cheng, K. L. Seyler, D. Zhong, E. Schmidgall, M. A. McGuire, D. H. Cobden *et al.*, Layer-dependent ferromagnetism in a van der Waals crystal down to the monolayer limit, Nature (London) **546**, 270 (2017).

[3] Z. Fei, B. Huang, P. Malinowski, W. Wang, T. Song, J. Sanchez, W. Yao, D. Xiao, X. Zhu, A. F. May *et al.*, Two-dimensional itinerant ferromagnetism in atomically thin Fe_3GeTe_2, Nat. Mater. **17**, 778 (2018).

[4] Y. Deng, Y. Yu, Y. Song, J. Zhang, N. Z. Wang, Z. Sun, Y. Yi, Y. Z. Wu, S. Wu, J. Zhu *et al.*, Gate-tunable room-temperature ferromagnetism in two-dimensional Fe_3GeTe_2, Nature (London) **563**, 94 (2018).

[5] Z. Wang, M. Gibertini, D. Dumcenco, T. Taniguchi, K. Watanabe, E. Giannini, and A. F. Morpurgo, Determining the phase diagram of atomically thin layered antiferromagnet $CrCl_3$, Nat. Nanotechnol. **14**, 1116 (2019).

[6] M. M. Otrokov, I. I. Klimovskikh, H. Bentmann, D. Estyunin, A. Zeugner, Z. S. Aliev, S. Gaß, A. U. B. Wolter, A. V. Koroleva, A. M. Shikin *et al.*, Prediction and observation of an antiferromagnetic topological insulator, Nature (London) **576**, 416 (2019).

[7] N. D. Mermin and H. Wagner, Absence of Ferromagnetism or Antiferromagnetism in One- or Two-Dimensional Isotropic Heisenberg Models, Phys. Rev. Lett. **17**, 1133 (1966).

[8] J. He, X. Li, P. Lyu, and P. Nachtigall, Near-room-temperature Chern insulator and Dirac spin-gapless semiconductor: Nickel chloride monolayer, Nanoscale **9**, 2246 (2017).

[9] X.-L. Sheng and B. K. Nikolić, Monolayer of the 5*d* transition metal trichloride $OsCl_3$: A playground for two-dimensional magnetism, room-temperature quantum anomalous Hall effect, and topological phase transitions, Phys. Rev. B **95**, 201402(R) (2017).

[10] Y. Li, Y. Liu, C. Wang, J. Wang, Y. Xu, and W. Duan, Electrically tunable valleytronics in quantum anomalous Hall insulating transition metal trihalides, Phys. Rev. B **98**, 201407(R) (2018).

[11] Z. Jiang, Y. Li, W. Duan, and S. Zhang, Half-Excitonic Insulator: A Single-Spin Bose-Einstein Condensate, Phys. Rev. Lett. **122**, 236402 (2019).

[12] M. Weisheit, S. Fähler, A. Marty, Y. Souche, C. Poinsignon, and D. Givord, Electric field-induced modification of magnetism in thin-film ferromagnets, Science **315**, 349 (2007).

[13] Z. Zhang, J.-Y. You, B. Gu, and G. Su, Antiferromagnetic and electric polarized states in two-dimensional Janus semiconductor $Fe_2Cl_3I_3$, J. Phys. Chem. C **124**, 19219 (2020).

[14] J.-Y. You, X.-J. Dong, B. Gu, and G. Su, Electric field induced topological phase transition and large enhancements of spin-orbit coupling and Curie temperature in two-dimensional ferromagnetic semiconductors, Phys. Rev. B **103**, 104403 (2021).

[15] X. Sui, T. Hu, J. Wang, B.-L. Gu, W. Duan, and M.-s. Miao, Voltage-controllable colossal magnetocrystalline anisotropy in single-layer transition metal dichalcogenides, Phys. Rev. B **96**, 041410(R) (2017).

[16] B. Huang, G. Clark, D. R. Klein, D. MacNeill, E. Navarro-Moratalla, K. L. Seyler, N. Wilson, M. A. McGuire, D. H. Cobden, D. Xiao *et al.*, Electrical control of 2D magnetism in bilayer CrI_3, Nat. Nanotechnol. **13**, 544 (2018).

[17] S. Jiang, J. Shan, and K. F. Mak, Electric-field switching of two-dimensional van der Waals magnets, Nat. Mater. **17**, 406 (2018).

[18] L. Webster and J.-A. Yan, Strain-tunable magnetic anisotropy in monolayer $CrCl_3$, $CrBr_3$, and CrI_3, Phys. Rev. B **98**, 144411 (2018).

[19] Z. Wu, J. Yu, and S. Yuan, Strain-tunable magnetic and electronic properties of monolayer CrI_3, Phys. Chem. Chem. Phys. **21**, 7750 (2019).

[20] A. M. León, J. W. González, J. Mejía-López, F. Crasto de Lima, and E. Suárez Morell, Strain-induced phase transition in CrI_3 bilayers, 2D Mater. **7**, 035008 (2020).

[21] X.-J. Dong, J.-Y. You, B. Gu, and G. Su, Strain-Induced Room-Temperature Ferromagnetic Semiconductors with Large Anomalous Hall Conductivity in Two-Dimensional $Cr_2Ge_2Se_6$, Phys. Rev. Applied **12**, 014020 (2019).

[22] Y. Li, Z. Jiang, J. Li, S. Xu, and W. Duan, Magnetic anisotropy of the two-dimensional ferromagnetic insulator $MnBi_2Te_4$, Phys. Rev. B **100**, 134438 (2019).

[23] C. K. Singh and M. Kabir, Long-range anisotropic Heisenberg ferromagnets and electrically tunable ordering, Phys. Rev. B **103**, 214411 (2021).

[24] T. Mukherjee, S. Chowdhury, D. Jana, and L. C. L. Y. Voon, Strain induced electronic and magnetic properties of 2D magnet CrI_3: A DFT approach, J. Phys.: Condens. Matter **31**, 335802 (2019).

[25] S. I. Vishkayi, Z. Torbatian, A. Qaiumzadeh, and R. Asgari, Strain and electric-field control of spin-spin interactions in monolayer CrI_3, Phys. Rev. Mater. **4**, 094004 (2020).

[26] C. Bacaksiz, D. Šabani, R. M. Menezes, and M. V. Milošević, Distinctive magnetic properties of CrI_3 and $CrBr_3$ monolayers caused by spin-orbit coupling, Phys. Rev. B **103**, 125418 (2021).

[27] Z. Zhang, J.-Y. You, B. Gu, and G. Su, Emergent magnetic states due to stacking and strain in the van der Waals magnetic trilayer CrI_3, Phys. Rev. B **104**, 174433 (2021).

[28] F. Zheng, J. Zhao, Z. Liu, M. Li, M. Zhou, S. Zhang, and P. Zhang, Tunable spin states in the two-dimensional magnet CrI_3, Nanoscale **10**, 14298 (2018).

[29] M. Pizzochero and O. V. Yazyev, Inducing magnetic phase transitions in monolayer CrI_3 via lattice deformations, J. Phys. Chem. C **124**, 7585 (2020).

[30] W. Chen, Z. Sun, Z. Wang, L. Gu, X. Xu, S. Wu, and C. Gao, Direct observation of van der Waals stacking–dependent interlayer magnetism, Science **366**, 983 (2019).

[31] N. A. Spaldin, *Magnetic Materials: Fundamentals and Device Applications* (Cambridge University Press, Cambridge, 2003).

[32] Y. Zhu, X. Kong, T. D. Rhone, and H. Guo, Systematic search for two-dimensional ferromagnetic materials, Phys. Rev. Mater. **2**, 081001(R) (2018).

[33] J. Liu, Q. Sun, Y. Kawazoe, and P. Jena, Exfoliating biocompatible ferromagnetic Cr-trihalide monolayers, Phys. Chem. Chem. Phys. **18**, 8777 (2016).

[34] S. V. Halilov, H. Eschrig, A. Y. Perlov, and P. M. Oppeneer, Adiabatic spin dynamics from spin-density-functional theory: Application to Fe, Co, and Ni, Phys. Rev. B **58**, 293 (1998).

[35] Y. Fang, S. Wu, Z.-Z. Zhu, and G.-Y. Guo, Large magneto-optical effects and magnetic anisotropy energy in two-dimensional $Cr_2Ge_2Te_6$, Phys. Rev. B **98**, 125416 (2018).

[36] K. Wang, X. Xu, Y. Cheng, M. Zhang, J.-S. Wang, H. Wang, and G. Zhang, Magnon-magnon interaction and magnon relaxation time in a ferromagnetic $Cr_2Ge_2Te_6$ monolayer, Phys. Rev. B **102**, 235434 (2020).

[37] W.-B. Zhang, Q. Qu, P. Zhu, and C.-H. Lam, Robust intrinsic ferromagnetism and half semiconductivity in stable two-dimensional single-layer chromium trihalides, J. Mater. Chem. C **3**, 12457 (2015).

[38] C. Huang, J. Feng, F. Wu, D. Ahmed, B. Huang, H. Xiang, K. Deng, and E. Kan, Toward intrinsic room-temperature ferromagnetism in two-dimensional semiconductors, J. Am. Chem. Soc. **140**, 11519 (2018).

[39] X. Lu, R. Fei, and L. Yang, Curie temperature of emerging two-dimensional magnetic structures, Phys. Rev. B **100**, 205409 (2019).

[40] A. Kabiraj, M. Kumar, and S. Mahapatra, High-throughput discovery of high Curie point two-dimensional ferromagnetic materials, npj Comput. Mater. **6**, 35 (2020).

[41] D. Torelli, K. S. Thygesen, and T. Olsen, High throughput computational screening for 2D ferromagnetic materials: The critical role of anisotropy and local correlations, 2D Mater. **6**, 045018 (2019).

[42] D. Torelli, H. Moustafa, K. W. Jacobsen, and T. Olsen, High-throughput computational screening for two-dimensional magnetic materials based on experimental databases of three-dimensional compounds, npj Comput. Mater. **6**, 158 (2020).

[43] Z. Wu, Z. Shen, Y. Xue, and C. Song, Strain-induced topological phase transition and enhanced Curie temperature in $MnBi_2Te_4/CrI_3$ heterojunction, Phys. Rev. Mater. **6**, 014011 (2022).

[44] N. Liu, S. Zhou, and J. Zhao, High-Curie-temperature ferromagnetism in bilayer CrI_3 on bulk semiconducting substrates, Phys. Rev. Mater. **4**, 094003 (2020).

[45] G.-D. Zhao, X. Liu, T. Hu, F. Jia, Y. Cui, W. Wu, M.-H. Whangbo, and W. Ren, Difference in magnetic anisotropy of the ferromagnetic monolayers VI_3 and CrI_3, Phys. Rev. B **103**, 014438 (2021).

[46] K. Shen, Finite temperature magnon spectra in yttrium iron garnet from a mean field approach in a tight-binding model, New J. Phys. **20**, 043025 (2018).

[47] V. V. Mkhitaryan and L. Ke, Self-consistently renormalized spin-wave theory of layered ferromagnets on the honeycomb lattice, Phys. Rev. B **104**, 064435 (2021).

[48] M. Bloch, Magnon Renormalization in Ferromagnets Near the Curie Point, Phys. Rev. Lett. **9**, 286 (1962).

[49] P. D. Loly, The Heisenberg ferromagnet in the selfconsistently renormalized spin wave approximation, J. Phys. C: Solid State Phys. **4**, 1365 (1971).

[50] E. Rastelli, A. Tassi, and L. Reatto, Selfconsistently renormalized spin-wave approximation for some two-dimensional magnetic systems, J. Phys. C: Solid State Phys. **7**, 1735 (1974).

[51] J. L. Lado and J. Fernández-Rossier, On the origin of magnetic anisotropy in two dimensional CrI_3, 2D Mater. **4**, 035002 (2017).

[52] Z. Li, T. Cao, and S. G. Louie, Two-dimensional ferromagnetism in few-layer van der Waals crystals: Renormalized spin-wave theory and calculations, J. Magn. Magn. Mater. **463**, 28 (2018).

[53] F. Xue, Y. Hou, Z. Wang, and R. Wu, Two-dimensional ferromagnetic van der Waals $CrCl_3$ monolayer with enhanced anisotropy and Curie temperature, Phys. Rev. B **100**, 224429 (2019).

[54] C. Song, W. Xiao, L. Li, Y. Lu, P. Jiang, C. Li, A. Chen, and Z. Zhong, Tunable band gap and enhanced ferromagnetism by surface adsorption in monolayer $Cr_2Ge_2Te_6$, Phys. Rev. B **99**, 214435 (2019).

[55] M. Shiranzaei, R. E. Troncoso, J. Fransson, A. Brataas, and A. Qaiumzadeh, Thermal squeezing and nonlinear spectral shift of magnons in antiferromagnetic insulators, New J. Phys. **24**, 103009 (2022).

[56] C. Kittel and C.-y. Fong, *Quantum Theory of Solids* (Wiley, New York, 1987).

[57] L.-S. Xie, G.-X. Jin, L. He, G. E. W. Bauer, J. Barker, and K. Xia, First-principles study of exchange interactions of yttrium iron garnet, Phys. Rev. B **95**, 014423 (2017).

[58] S. Bertolazzi, J. Brivio, and A. Kis, Stretching and breaking of ultrathin MoS_2, ACS Nano **5**, 9703 (2011).

[59] G. Kresse and J. Hafner, *Ab initio* molecular dynamics for liquid metals, Phys. Rev. B **47**, 558 (1993).

[60] G. Kresse and J. Furthmüller, Efficient iterative schemes for *ab initio* total-energy calculations using a plane-wave basis set, Phys. Rev. B **54**, 11169 (1996).

[61] J. P. Perdew, K. Burke, and M. Ernzerhof, Generalized Gradient Approximation Made Simple, Phys. Rev. Lett. **77**, 3865 (1996).

[62] G. Kresse and D. Joubert, From ultrasoft pseudopotentials to the projector augmented-wave method, Phys. Rev. B **59**, 1758 (1999).

[63] P. E. Blöchl, Projector augmented-wave method, Phys. Rev. B **50**, 17953 (1994).

[64] H. J. Monkhorst and J. D. Pack, Special points for Brillouin-zone integrations, Phys. Rev. B **13**, 5188 (1976).

[65] H. Wang, F. Fan, S. Zhu, and H. Wu, Doping enhanced ferromagnetism and induced half-metallicity in CrI_3 monolayer, Europhys. Lett. **114**, 47001 (2016).

[66] L. Ren, Q. Liu, P. Xu, Z. Zhong, L. Yang, Z. Yuan, and K. Xia, Noncollinearity-modulated electronic properties of monolayer CrI_3, Phys. Rev. Appl. **11**, 054042 (2019).

[67] R. Peng, H. C. Xu, S. Y. Tan, H. Y. Cao, M. Xia, X. P. Shen, Z. C. Huang, C. Wen, Q. Song, T. Zhang *et al.*, Tuning the band structure and superconductivity in single-layer FeSe by interface engineering, Nat. Commun. **5**, 5044 (2014).

[68] P. Zhang, X.-L. Peng, T. Qian, P. Richard, X. Shi, J.-Z. Ma, B. B. Fu, Y.-L. Guo, Z. Q. Han, S. C. Wang *et al.*, Observation of high-T_c superconductivity in rectangular $FeSe/SrTiO_3(110)$ monolayers, Phys. Rev. B **94**, 104510 (2016).

[69] P. Jiang, L. Li, Z. Liao, Y. X. Zhao, and Z. Zhong, Spin direction-controlled electronic band structure in two-dimensional ferromagnetic CrI_3, Nano Lett. **18**, 3844 (2018).

[70] L. Chen, J.-H. Chung, B. Gao, T. Chen, M. B. Stone, A. I. Kolesnikov, Q. Huang, and P. Dai, Topological Spin Excitations in Honeycomb Ferromagnet CrI_3, Phys. Rev. X **8**, 041028 (2018).

[71] L. Chen, J.-H. Chung, M. B. Stone, A. I. Kolesnikov, B. Winn, V. O. Garlea, D. L. Abernathy, B. Gao, M. Augustin, E. J. G. Santos, and P. Dai, Magnetic Field Effect on Topological Spin Excitations in CrI_3, Phys. Rev. X **11**, 031047 (2021).

[72] T. Holstein and H. Primakoff, Field Dependence of the Intrinsic Domain Magnetization of a Ferromagnet, Phys. Rev. **58**, 1098 (1940).

[73] M.-w. Xiao, Theory of transformation for the diagonalization of quadratic Hamiltonians, arXiv:0908.0787 [math-ph].

[74] A. Cong, J. Liu, W. Xue, H. Liu, Y. Liu, and K. Shen, Exchange-mediated magnon-phonon scattering in monolayer CrI_3, Phys. Rev. B **106**, 214424 (2022).

[75] D. Torelli and T. Olsen, Calculating critical temperatures for ferromagnetic order in two-dimensional materials, 2D Mater. **6**, 015028 (2018).

[76] B. Wei, J.-J. Zhu, Y. Song, and K. Chang, Renormalization of gapped magnon excitation in monolayer $MnBi_2Te_4$ by magnon-magnon interaction, Phys. Rev. B **104**, 174436 (2021).

[77] N. W. Ashcroft and N. D. Mermin, *Solid State Physics* (Holt-Saunders, Philadelphia, 1976).

[78] Y. Xue, Z. Shen, Z. Wu, and C. Song, Theoretical prediction of curie temperature in two-dimensional ferromagnetic monolayer, J. Appl. Phys. **132**, 053901 (2022).

[79] S. Jiang, L. Li, Z. Wang, K. F. Mak, and J. Shan, Controlling magnetism in 2D CrI_3 by electrostatic doping, Nat. Nanotechnol. **13**, 549 (2018).

[80] W. Su, Z. Zhang, Q. Cao, D. Wang, H. Lu, W. Mi, and Y. Du, Enhancing the curie temperature of two-dimensional monolayer CrI_3 by introducing I-vacancies and interstitial H-atoms, Phys. Chem. Chem. Phys. **23**, 22103 (2021).

[81] M. Lu, Q. Yao, Q. Li, C. Xiao, C. Huang, and E. Kan, Tuning electronic and magnetic properties of two-dimensional ferromagnetic semiconductor CrI_3 through adsorption of benzene, J. Phys. Chem. C **124**, 22143 (2020).

[82] M. Rassekh, J. He, S. F. Shayesteh, and J. J. Palacios, Remarkably enhanced Curie temperature in monolayer CrI_3 by hydrogen and oxygen adsorption: A first-principles calculations, Comput. Mater. Sci. **183**, 109820 (2020).

[83] Q. Yang, X. Hu, X. Shen, A. V. Krasheninnikov, Z. Chen, and L. Sun, Enhancing ferromagnetism and tuning electronic properties of CrI_3 monolayers by adsorption of transition-metal atoms, ACS Appl. Mater. Interfaces **13**, 21593 (2021).